Diamond & Related Materials 130 (2022) 109482

Contents lists available at ScienceDirect

Diamond & Related Materials

journal homepage: www.elsevier.com/locate/diamond

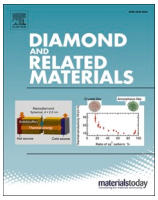

Stability of lithographically patterned transition metal layers controls spatial selectivity during etching of diamond

Zhijie Wang, M. Ravi Shankar *

Department of Industrial Engineering, Swanson School of Engineering, University of Pittsburgh, PA 15261, United States of America

ARTICLE INFO

Keywords:
Diamond
Diffusion
Transition metal
Surface structuring

ABSTRACT

Transition metals (TM) that are lithographically patterned on surfaces of polycrystalline diamond offer a vehicle for site selective removal of carbon. Here, we present a characterization of the trade-offs between spatial selectivity, isotropy of material removal and etching rate as a function of the TM composition and heat treatment. Fe, Co, Ni and FeCoB were studied for their ability to convert and transport C from diamond under heat treatment. Following solvothermal removal of the reaction products, the surface topographies inherited by diamond were characterized using atomic force microscopy. The structure of interaction zones between diamond and TM were studied using electron microscopy and Raman spectroscopy. Ni layers remain stable during the heat treatment to enable highly selective material removal. However, Fe, Co and FeCoB layers were fragmented and transported by the reaction products, which led to loss of selectivity in material removal. The etching rate of FeCoB shows a weaker dependency with diamond surface grain orientation. Combinatorial process designs involving bilayers of Ni and FeCoB enable trade-offs in the etching rate and isotropy, including the ability to control the side profiles of the etched features on diamond.

1. Introduction

The hardness of diamond facilitates its use as a cutting tool material in precision machining to create surface finishes with the nm-scale roughness [1–3]. This is a tradition that dates to at least the first millennium BCE [4]. Complementing its mechanical properties, diamond is also characterized by thermal stability [5], ultra-wide band gap [6,7], chemical inertness [8], and high thermal conductivity [9]. These property combinations unlock applications in power electronics [5,10,11], optical elements [12], and information processing [13]. Structuring diamond for engineered applications presents a challenge. Current approaches include reactive ion etching (RIE) [14,15], electron-beam-induced etching (EBIE) [16], inductively coupled plasma reactive ion etching (ICP-RIE) [17,18], laser machining [19], and focused ion beam milling (FIB) [20]. Typically, these approaches involve significant capital expenditures and are characterized by low machining rates using fluidic etchants, which place limitation on their applications. d-shell rich transition metals (TM) interact with diamond under high temperature (>800 °C), which can be harnessed as a subtractive manufacturing process [21–25]. Compared with existing (fluidic) dry or wet etchants, TM as solid state etchants present nascent advantages for etching diamond in terms of low cost and environmental safety [26]. The frameworks explored here obviate expensive capital equipment, which enables scalable production. Furthermore, TM etchants can be spatially localized on the target diamond surface in both horizontal and vertical mounting configuration with patterning that can approach nanoscale feature sizes. The ability to localize the solid state etchant also enables single-step hierarchical pattern fabrication by depositing multiple TM (that provide different etching rates) with spatial selectivity on diamond surfaces, which is desirable in fabricating devices with complex topographical architectures [7,10,11,27–30]. Often, the grain orientation dependence of the (anisotropic) etching rate limits its application, especially in polycrystalline diamond. Our previous work on selective patterning of polycrystalline diamond using lithographically deposited FeCoB [31] offers a microstructure-agnostic approach. However, fundamental understanding of the causes for the distortion of the features inherited from etching with TM remain to be elucidated.

Here, we explore a library of TM solid state etchants to define the trade-space of material removal rate versus the spatial specificity of the patterning inherited by diamond as a function of the process parameters. This was explored as a function of the thermal heat treatment that leads to the diffusion of C into the TM. The surface topography inherited by

* Corresponding author.
E-mail address: ravishm@pitt.edu (M.R. Shankar).

https://doi.org/10.1016/j.diamond.2022.109482
Received 3 July 2022; Received in revised form 30 September 2022; Accepted 17 October 2022
Available online 19 October 2022

diamond was characterized following solvothermal removal of the reaction products. The performance of Fe, Co, Ni and FeCoB was compared. The diamond etching rate, its orientation dependent anisotropy, spatial selectivity (distortion of the predefined profile and roughness following etching) was characterized. These responses were related to the structure of the interaction layer between diamond and the TM following heat treatment. Electron microscopy (Scanning Electron Microscopy; SEM and Transmission Electron Microscopy; TEM), atomic force microscope (AFM), and Raman spectroscopy was brought to bear on suitably prepared cross-sections of the interaction zone. Electron backscattered diffraction (EBSD) in the SEM was utilized to characterize the crystallographic texture. The underlying trade-offs between etching performance and specificity was delineated within the context of the structure and stability of the interaction zone. The composition of the solid-state etchant emerged as the primary determinant of the structure-property relationships. This characterization was also harnessed in hierarchically structured solid-state etchants to realize orientation agnostic, low distortion patterning of diamond. The understanding of underlying TM/diamond interaction mechanism is valuable for the design of diamond tools to increase their life in subtractive manufacturing processes such as diamond turning [32–34]. This approach is also a vehicle for modulating the side wall profiles of etched surfaces (e.g., etching along angles, instead of creating vertical edge profiles), which are useful for fabricating diamond-based quantum photonic devices [35], and superhydrophobic surfaces [36].

2. Experiment

2.1. Materials

The diamond samples used in this work were chemical vapor deposition (CVD) grown polycrystals manufactured by II-VI Infrared Co. The orientations of diamond grains on the surface are randomly distributed and no particularly preferred orientation or texture is observed (Fig. S1; EBSD micrograph). All chemical reagents (acetone, sulfuric acid, nitric acid) are of ACS certified grade. Transition metal sources used for thin film deposition have purities better than 99.9 % and were purchased from the Kurt J. Lesker Company. The Fe, Co, Ni sources for thin film deposition were commercially available targets, while the FeCoB was a premixed commercial target. The FeCoB, Co, and Ni thin films were deposited using an electron beam evaporator (Plassys MEB550S) with a deposition rate of 0.2 ± 0.01 nm/s in vacuum (chamber pressure $< 5 \times 10^{-7}$ mBar). Fe films were deposited via Physical Vapor Deposition (PVD) sputtering system (Angstrom Engineering Sputtering System) with a sputtering rate of 0.15 ± 0.02 nm/s in vacuum (chamber pressure $< 1 \times 10^{-6}$ mBar). The thickness of the TM films can be controlled with an accuracy of ±3 nm.

2.2. Characterization

Surface topographies of diamond samples before and after each treatment (deposition, annealing, and acid removal) were measured using an AFM (Veeco Multimode V). Orientation Imaging Microscopy (OIM) via EBSD was used to characterize the surface orientations of CVD diamond. This was performed on a FEI Apreo SEM with an EDAX EBSD camera. The chemical components of the interaction layer between diamond and transition metal (Ni and FeCoB) after annealing were characterized using energy-dispersive X-ray spectroscopy (EDAX) using an SEM (FEI Apreo), TEM (JEOL JEM-2100F), and Raman (Renishaw inVia). The electron transparent cross-sections for imaging the interaction layer were prepared by focused ion beam milling (FIB, FEI Scios DualBeam). The schematic of this process was shown in Fig. S2.

2.3. Selective patterning process

TM thin films were selectively deposited on polycrystalline diamond surface using photolithography and lift-off methods. The samples were then annealed under 800 °C for 90 min in a vacuum furnace. Evacuation was accomplished using a Pfeiffer Vacuum D-35614 Asslar TMH 071 P. The residual pressure during annealing was 1×10^{-6} mBar. Subsequently, the samples were solvothermally cleaned using a mixture (H_2SO_4:HNO_3 = 3:1 at volume ratio) under 220 °C for 30 min in a high-pressure reactor to remove all reaction products and metal residues. Finally, the samples were ultrasonically cleaned by DI water and acetone to remove acids and other containments.

3. Results and discussion

Four different solid etchants (Fe, Co, Ni, and FeCoB) were interacted with diamond substates at elevated temperatures. Solvothermal removal of the reaction products was used to reveal the etched topographies. Fig. 1(a)-(d) show the top view of surface topographies created with Fe, Co, Ni, and FeCoB alloy, respectively. We note the effect of the etching depths and the roughness of the etched diamond surface. Under comparable heat treatment conditions, FeCoB presents higher diamond removal (deeper etching) than pure Fe, Co, and Ni. However, the surface roughness of the diamond substrate etched with FeCoB is larger than that resulting from pure metals (Fe, Co, or Ni). Fig. 1(e)-(h) illustrate the effect of the TM etchant on the specificity of the material removal as a function of the composition. This was explored for creating 1 μm wide grooves with Fe, Co, Ni, and FeCoB, respectively. Among these four solid-state etchants, Ni etched diamond substrates with spatial selectivity that replicated the lithographically deposited pattern. The other systems show distortion at the edges of the profiles. We considered the relationship between the etching depth and the roughness within the etched region. For example, in Fig. S3, the roughness of the etched samples with different etching depths was explored as a function of the time of heat treatment with FeCoB. Fig. 1(i) illustrates the ratio of the roughness in the etched area to the etching depth with a given TM etchant. Ni shows the lowest ratio of roughness to etching depth, which is reflective of its ability to create low roughness surfaces, while presenting an etching depth that is much smaller than that with FeCoB. The Ra/depth ratio of FeCoB is just above that for Ni. Interestingly, although the Ra produced with Fe and Co are smaller than that for FeCoB, the ratio of Ra/depth is significantly higher. This is because of their modest etching rates in comparison to the other TM.

To understand the underlying mechanism of distortion in the etched profiles, we characterized the interaction layer between diamond and different transition metals. Fig. 2 (a)-(d) show the top views (SEM) of the diamond/transition metal surfaces after annealing (800 °C 90 min). Only nickel/diamond interaction layer maintained the original profile (and linear edges) of the as-deposited metal film (Fig. S4) after annealing. The interaction layers between diamond and Fe, Co, or FeCoB lost the clear and sharp boundaries of the as-deposited film and spread out laterally, beyond their prior confines. The dispersion of the reaction products and the inability to localize the TM etchants reflects the distorted edges in the AFM micrographs of etched diamond after the solvothermal, chemical removal of the reaction products (Fig. 1). The Raman spectroscopy results of the diamond sample as shown in Fig. S5 and our previous work [31] confirms the complete removal of the reaction products.

The structure of the diffusional interaction layer was characterized using TEM. Fig. 2 (e)-(h) shows TEM images of the cross sections of diamond/TM interaction zone. The samples were prepared by focus ion beam milling (FIB) as illustrated in Fig. S2. The imaging orientation in the TEM using the bright field mode were perpendicular to the cross-section of the diamond/TM interaction interface in the as-prepared FIB samples. The bright field images of the diffusional interaction zones show a matrix of low contrast regions within which islands of dark contrast (marked with red arrows) are interspersed. Based on the EDS scanning and Raman Spectroscopy results, as shown in Figs. S6 (d) and S7 [31], the dark islands are TM rich while the low contrast regions are

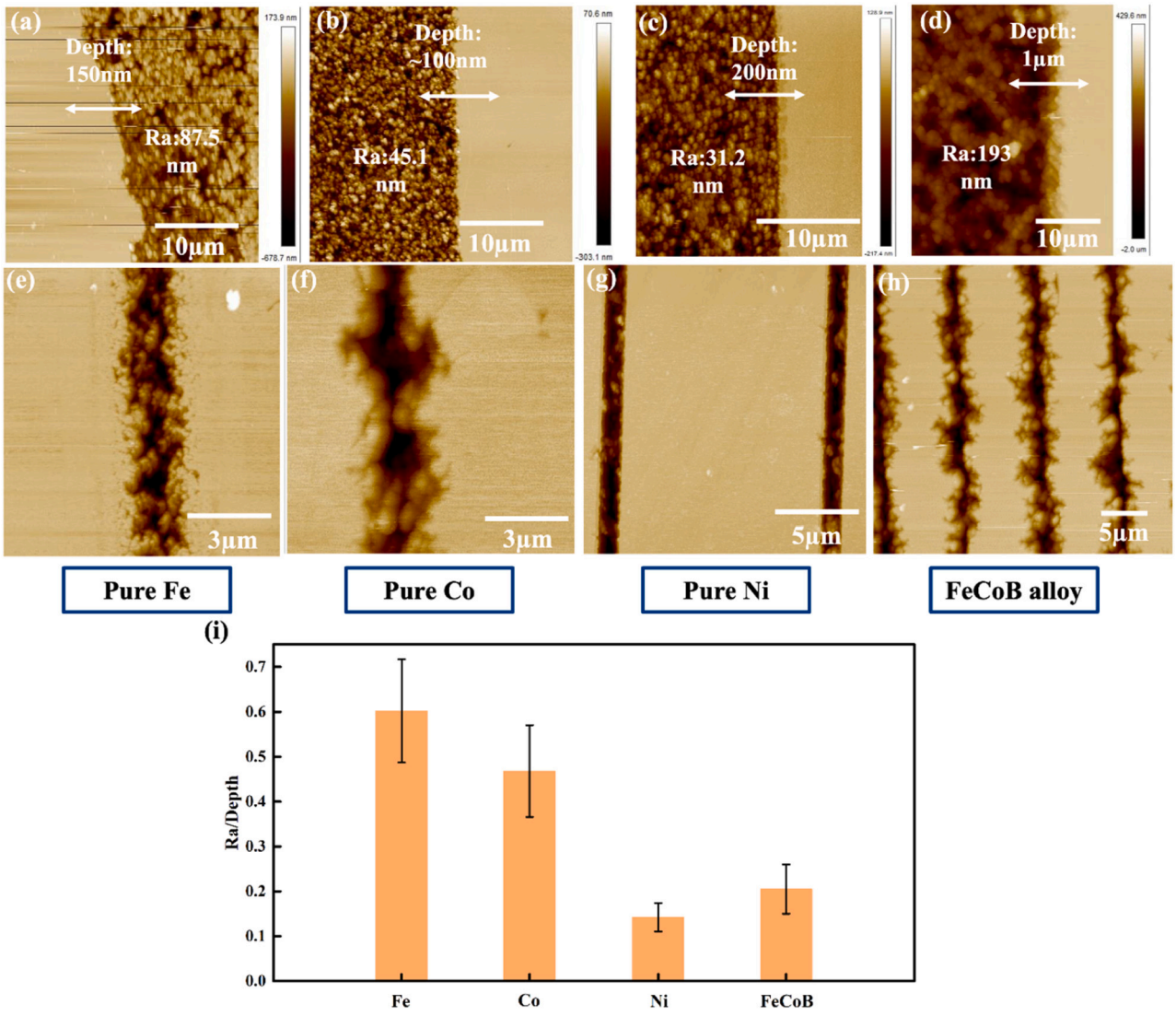

Fig. 1. Etching diamond via interaction with TM and removal of reaction products via solvothermal treatment. AFM micrographs of diamond after reaction production removal, which indicate roughness and etching depths etched by (a) Fe, (b) Co, (c) Ni, and (d) FeCoB. The etched profiles inherited from the TM profiles generated with (e) Fe, (f) Co, (g) Ni, and (h) FeCoB; (i) ratio of surface roughness to etching depth among different solid-state etchants.

sp^2 carbon. Among the various solid-state etchants, only Ni layer stayed integral at diamond/diffusion layer boundary (i.e., retained its as-deposited profile) after thermal interaction with diamond, as shown in Fig. 2 (g). This is consistent with the observation in Fig. 2 (c). Fe, Co, and FeCoB alloy phases were disrupted and relocated to the top of the sp^2 carbon layer, as shown in Fig. 2 (e), (f), and (h). The TEM images and selected area electron diffraction (SAED) results of the as-deposited Ni layer (Fig. S8) show a nanocrystalline structure. As do other as-deposited transition metal layers [31].

The diffusional interaction between diamond and transition metals (Fe, Co, Ni, or FeCoB) are initiated when the temperature reaches ~800 °C. The mechanism of C removal is schematized in Fig. 3 (a)→(b)→(e)→(f). The carbon atoms segregate at the transition metal (Fe, Co, or FeCoB) grain boundaries, which accelerates its fragmentation. Carbon rich particles inhabit the TM layers in contact with the diamond and carbon poor islands are distributed further away from the diamond/TM interface. The diffusional interaction between diamond and Ni stands in contrast to this behavior. The Ni layer remains predominantly intact during the heat treatment process and continuously transforms diamond into sp^2 carbon. The deposited Ni has a nanocrystalline structure, which remains ultrafine after annealing, as shown in Fig. S6 (b) and (c). The stability of Ni layer is attributed to its lower grain boundary energy that prevents disruption of its structure from carbon segregation. Combined with the etching distortion results shown in Fig. 1, it confirms the stability of TM layer during whole heat treatment process is the key to ensuring site-selective material removal.

The effect of the orientation of diamond on the material removal is an important factor that determines the ability to controllably pattern surfaces using such diffusion interactions. In general, an etchant with weaker anisotropy is preferable. We measured the etching depths on diamond with different surface orientation annealed with 100 nm thick transition metals under 800 °C for 90 min, the results are shown in Fig. 4. Fe, Co, and Ni show strongly anisotropic etching on different underlying diamond grain orientations. However, Ni shows a highly site-selective material removal due to the stability of the Ni on the diamond surface. Diamond orientation close to {111} has the lowest etching rate while the orientation close to {101} has the highest etching rate using Fe, Co, or Ni as etchants. FeCoB not only shows a much faster etching rate than Fe, Co, and Ni at any orientations, but also has a weaker diamond grain orientation dependency. However, FeCoB has a related lower etching rate when the diamond orientation is close to {001} or {101}, which is in contrast to that in Fe, Co, or Ni.

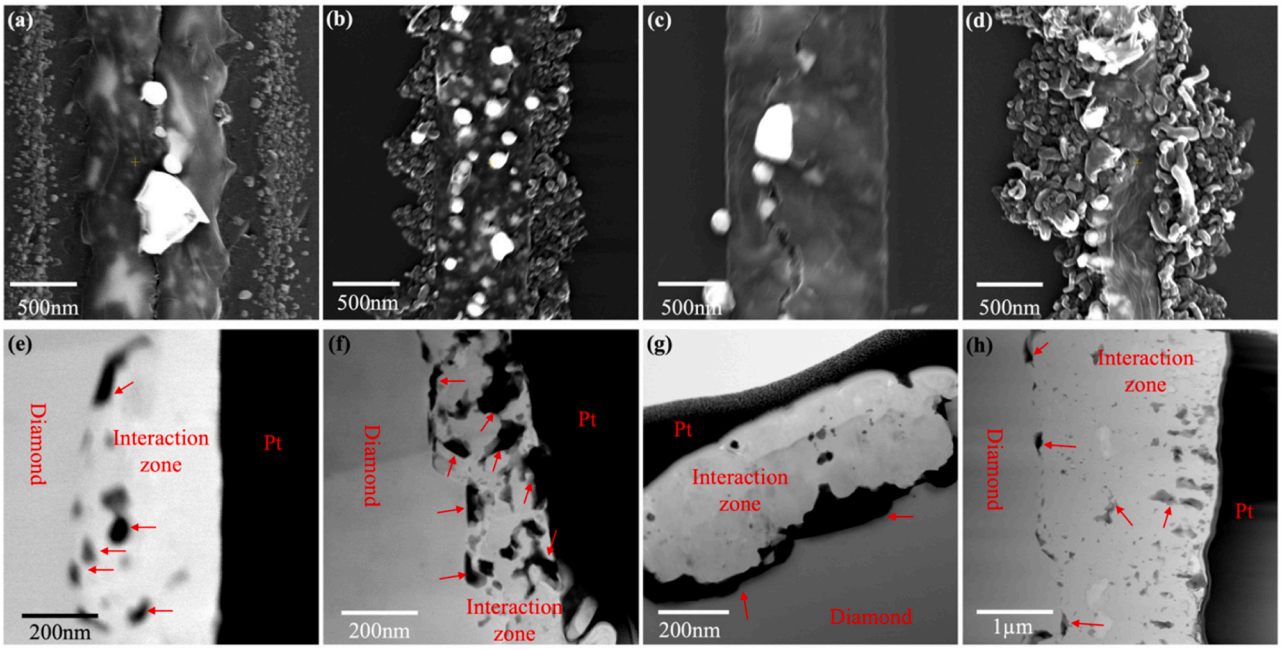

Fig. 2. Structure of diamond/transition-metal interaction zone. SEM images of the top view of the interaction zone between diamond and 100 nm thick (a) Fe, (b) Co, (c) Ni, (d) FeCoB films after 800 °C 90 min annealing; TEM images of the cross-section of the interaction zone between diamond and (e) Fe, (f) Co, (g) Ni, (h) FeCoB films after 800 °C 90 min annealing.

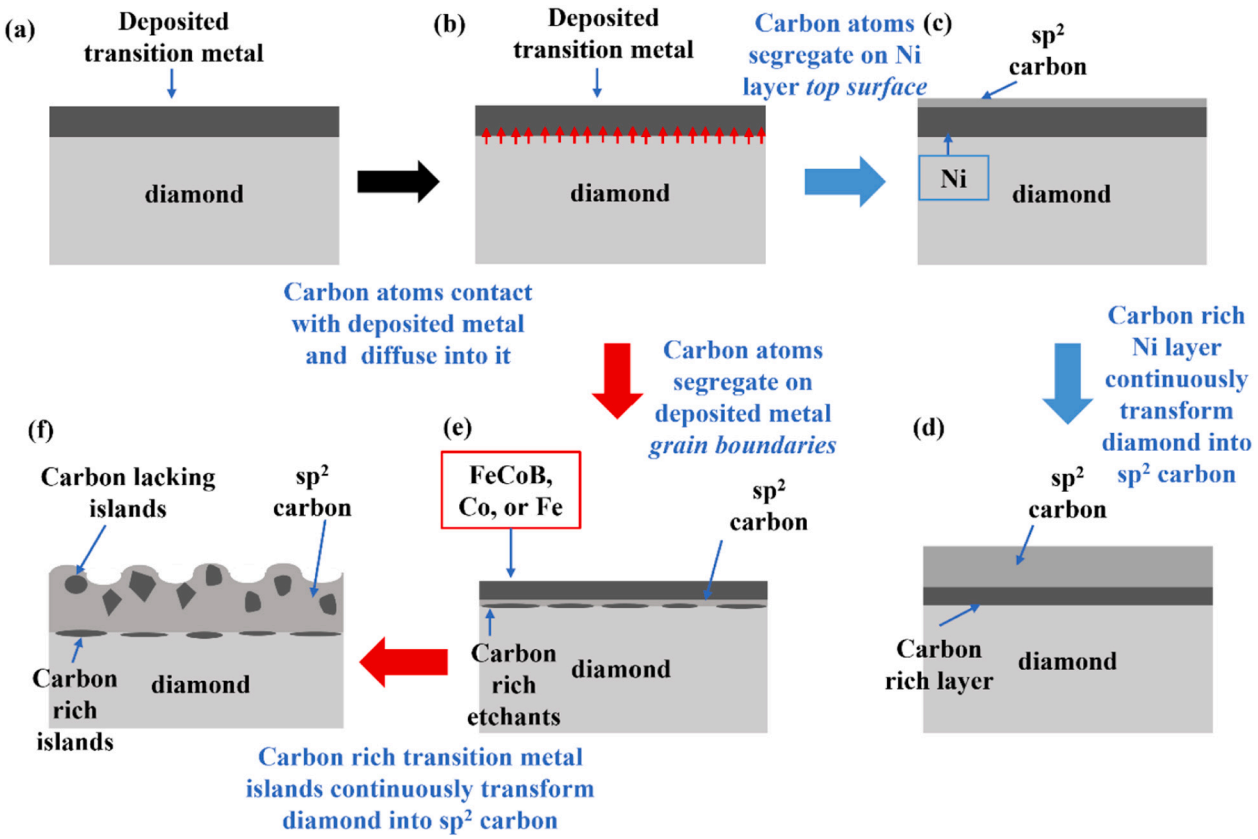

Fig. 3. Schematic of the diffusion-based removal of C from diamond substrates using TM. (a) → (b) → (c) → (d) Ni, and (a) → (b) → (e) → (f) FeCoB, Co, or Fe.

The etching rate (carbon transport rate) is limited by three major processes: i) the breaking of diamond back bonds, ii) the diffusion of carbon in transition metals, and iii) the segregation of carbon at the grain boundaries of bottom layer transition metals. The reaction rate of breaking diamond back bonds (R_1) is a characteristic Arrhenius equation: $R_1 = Ae^{-\frac{E}{kT}}$. E is the activation energy to break back-bonds of diamond, T is temperature, A and k are constants. Diamond's grain orientation is one of the major determinants of the activation energy E

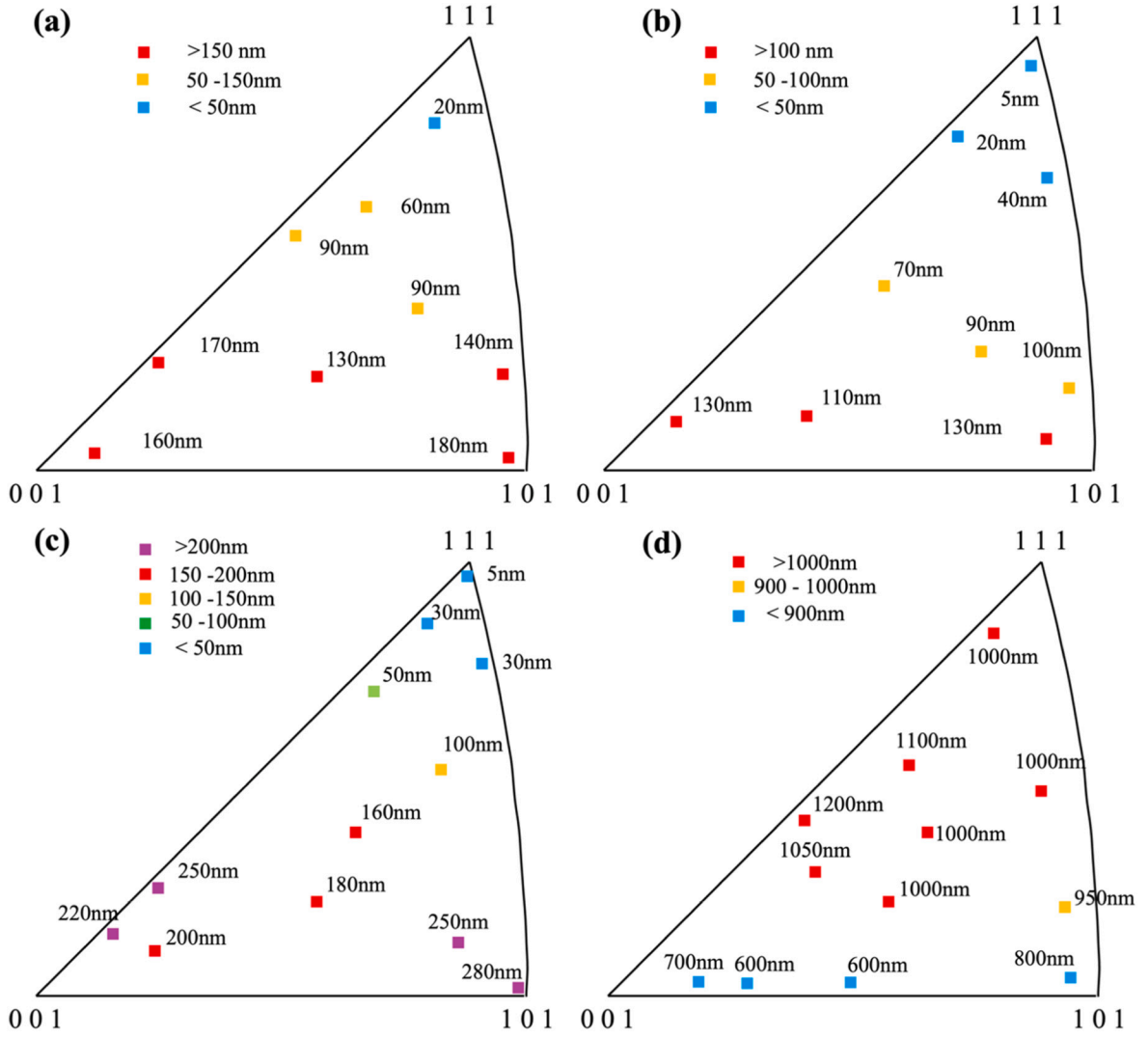

Fig. 4. Etching depths on diamond as a function of orientations using (a) Fe, (b) Co, (c) Ni, and (d) FeCoB as a result of heat treatment at 800 °C for 90 min. This was followed by solvothermal etching to remove reaction products.

[24]. For Fe, Co, or Ni, the carbon removal process at {111} must occur layer by layer. To remove atom B (shown in the Fig. 5), atom A must be removed first. The activation energy of removing atom A from atom B layer is much higher than that for removing carbon at either {110} or {100} plane. This limits the carbon removal rate (etching rate) among {111} plane [24]. FeCoB likely removes carbon at {111} planes in an accelerated manner. Here, the disruption of the back bonds (atom B) can proceed independent of those for the bonds of atom A. That is, the back bonds of atom B are broken while the back bonds of atom A are still intact, as shown in the red dashes in Fig. 5. Since Fe or Co show similar etching manner with Ni, this can occur due to a change in the FeCoB lattice and its interaction with diamond due to boron [37,38], and the diffusion of boron into diamond [39]. These allow the back bonds of atom B to break prior to the disruption of those for atom A (due to the higher activation energy required to break those of A) [24]. The activation energy of breaking back bonds of atom B at {111} has lower the active energy of breaking back bonds at either {110} or {100} [40,41], which makes FeCoB have an inverse etching rate/diamond grain orientation in comparison to Fe, Co, or Ni. This can contribute to its higher carbon removal efficiency. In addition, due to the faster rate of breaking of back bonds by FeCoB (expected at orientations very close to {110} or {100}), the etching rate will be limited by the rate of diffusion of carbon into the matrix (R_2) or the precipitation of carbon at the grain

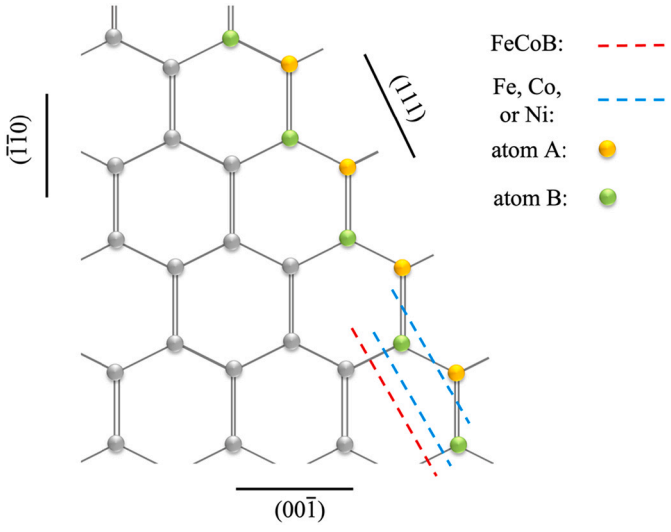

Fig. 5. 2D projection of diamond lattice and the schematic of multiple pathways of bond breaking and carbon removal at {111} planes. This is an adaptation of the idea in Ref. [24].

boundaries of bottom layer transition metals (R_3). R_2 and R_3 are diamond orientation independent. It is this disparity that makes FeCoB's etching rate less sensitive to the diamond's microstructure, while that of Fe, Co or Ni remains highly sensitive to it.

To combine the advantages of Ni (lower edge distortion) and FeCoB (higher etching rate and weaker diamond orientation dependency), we designed a hierarchical solid-state diamond etchant. Fig. 6 (a) shows the schematic of the design of the Ni-FeCoB etchant. A 50 nm thick Ni film was deposited on the masked diamond sample followed by the deposition of a 50 nm FeCoB film on top of Ni. Both materials are deposited using e-beam evaporation. Fig. 6 (b) and (c) shows the AFM images of Ni-FeCoB etched surface. The etching depth is 800 nm (higher than Fe, Co, or Ni) while the etching distortion is milder than FeCoB. Fig. 6 (d) shows the SEM top view image of the diamond/Ni + FeCoB interaction zone after 800 °C 90 min annealing. The interaction zone remained localized to its as-deposited shape on the diamond surface. This is due to the stabilizing effect of Ni during the annealing. Meanwhile, this Ni-FeCoB etchant inherits the accelerated etching due to FeCoB.

This approach was also adapted for etching diamond along a sloped profile. The schematic of the material and process design are shown in Fig. 7(a). A Ni layer was deposited on the top of diamond substrate by e-beam evaporation at first, followed by selected area deposition of a FeCoB film by lift-off process. After that, the sample was annealed at 650 °C to initiate boron's (FeCoB) diffusion into the Ni middle layer (Ni/FeCoB does not react with diamond at this temperature [31]). Subsequently, the sample was annealed under 800 °C for 90 min, to induce the interaction of diamond and transition metals. The concentration of boron (from the FeCoB) in the Ni middle layer will follow a graded diffusion driven profile as a function of the interdiffusion time and temperature. Transport of B is particularly accelerated with its diffusion coefficient in Ni of 2.6×10^{-12} m^2/s at 650 °C [42]. Boron's effect in magnifying C removal would occur in a graded fashion, which will result in regions of Ni in the vicinity of FeCoB islands showing a higher rate of diamond etching in comparison to those further from the islands. Fig. 7 (b) and (c) the etching of diamond along a sloped (graded profile). The thickness of Ni and FeCoB films are 100 nm and 80 nm, where the low

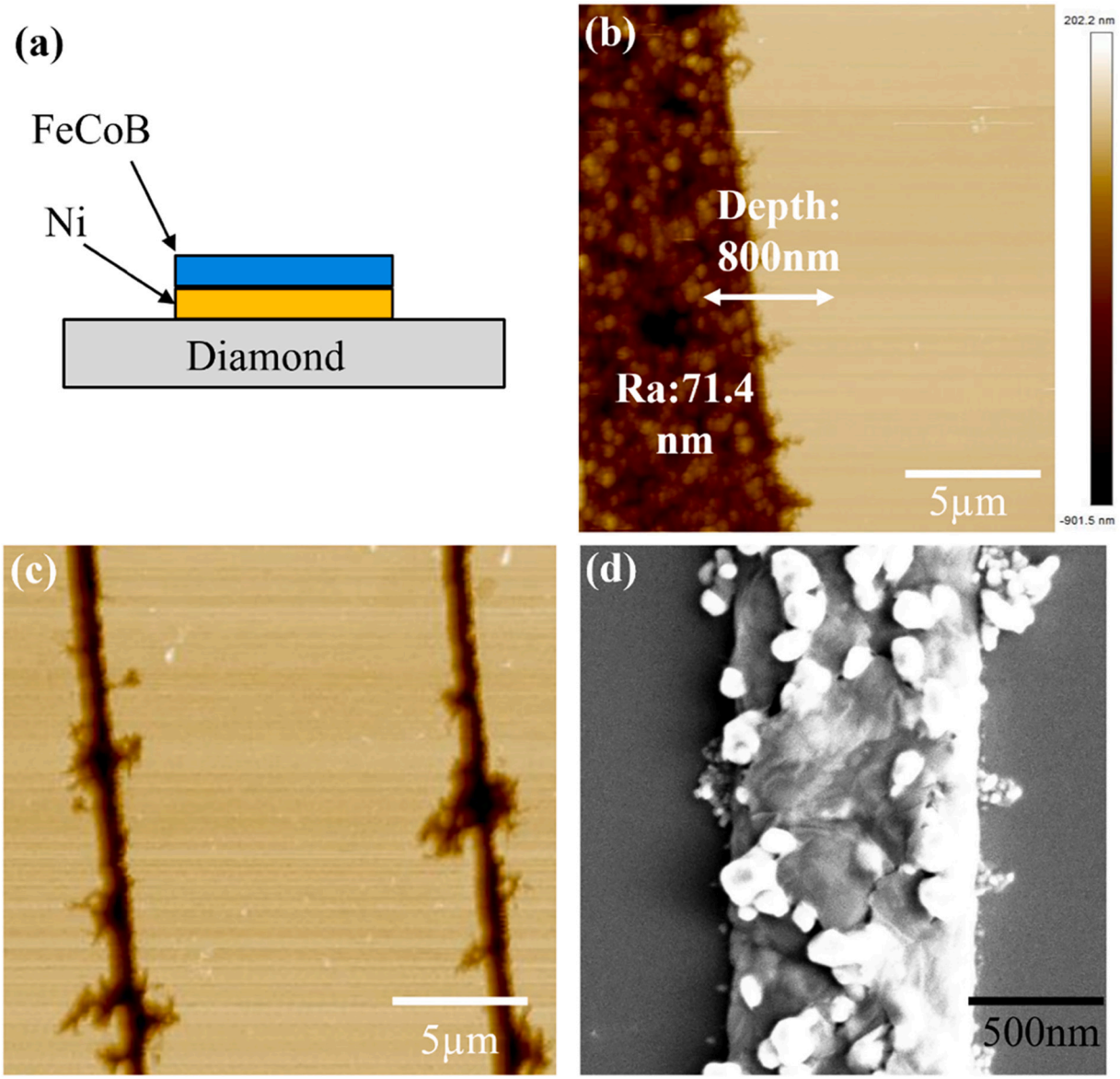

Fig. 6. Diamond etching with a Ni-FeCoB hierarchical etchant. The samples were annealed under 800 °C for 90 min in vacuum. (a) Schematic of the Ni-FeCoB etchant. b) AFM top view of the diamond sample etched by Ni-FeCoB etchants after solvothermal removal of reaction products. Etched area roughness and etching depths are shown. c) Distortion of the edge of the patterns. (d) SEM images of the top view of the interaction zone between diamond and Ni-FeCoB before solvothermal removal of the reaction products (50 nm Ni + 50 nm FeCoB).

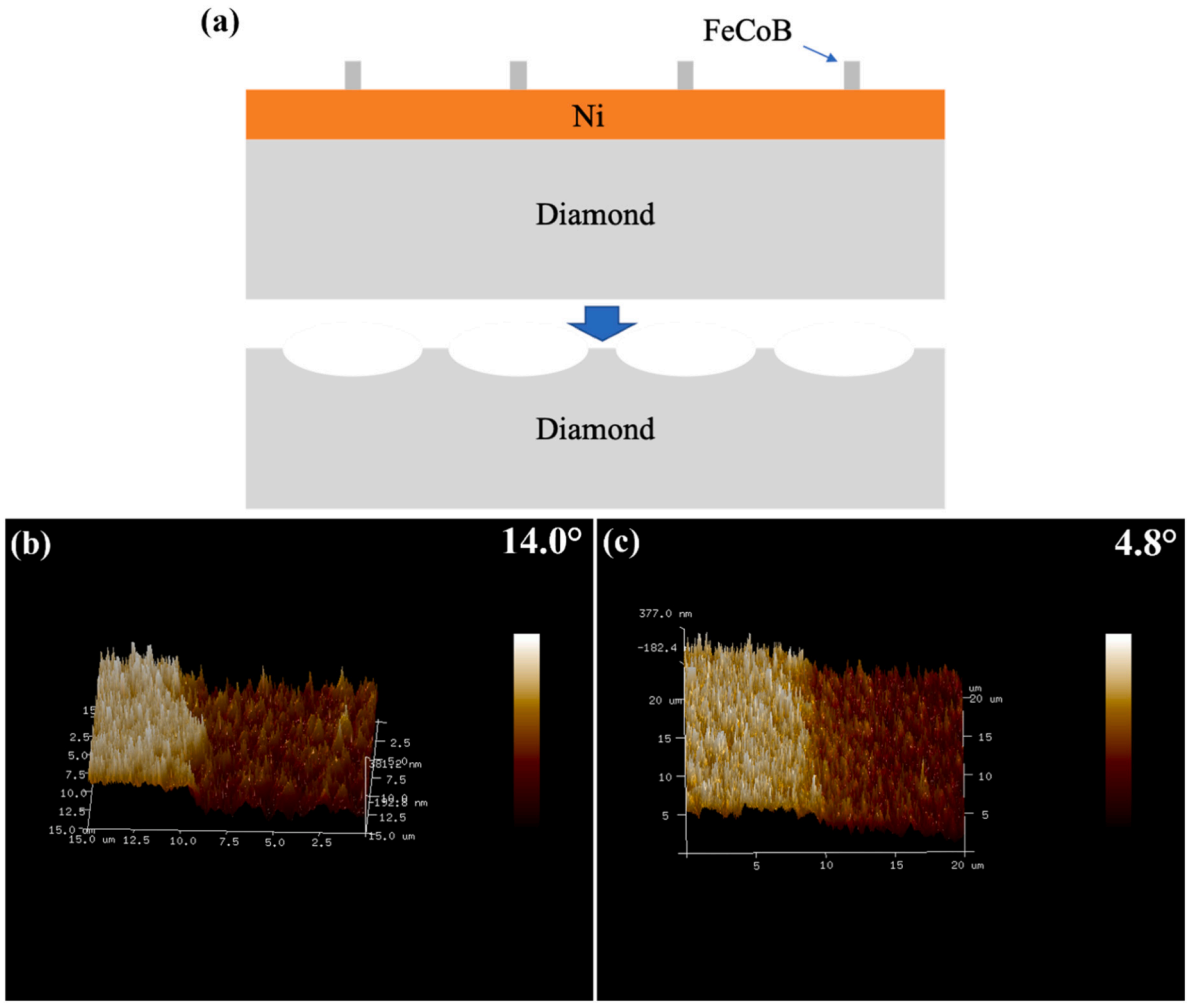

Fig. 7. Controlling the slope of the sidewalls of features created on diamond using a Ni-FeCoB hierarchical etchant. (a) Schematic of the Ni-FeCoB hierarchical etchant. AFM images of the obliquely etched diamond using a 100 nm Ni middle layer and an 80 nm FeCoB top layer annealed at 650 °C for (b) 50 min and (c) 100 min followed by a high temperature annealed at 800 °C 90 min. AFM scans were performed after solvothermal removal of the reaction products.

temperature annealing is processed at 650 °C for 50 min (Fig. 7b) and 100 min (Fig. 7c). As can be seen, the angle between the sloped wall of the etched area and diamond surface is 14.0° when the low temperature annealing time is 50 min and decreased to 4.8° when the low temperature annealing time increases to 100 min. This idea was also explored using Fe and Co as the middle layer, with a FeCoB layer atop it (Fig. S9). The observations here correspond to that in the Ni-FeCoB system, which suggests a broader combinatorial motif for controlling the sidewall profiles of features resulting from solid state etching of diamond with TM.

4. Conclusions

The trade-space of etching rate vs. site specificity during etching of diamond using lithographically patterned transition metals was outlined. The performance of Fe, Co, Ni and FeCoB was explored. The topographies of diamond etched by different transition metals were measured using AFM and the corresponding distortion were recorded. The microstructure of the corresponding interaction zones was characterized using TEM, SEM, EDS and Raman spectroscopy. We show that the key factor determining the specificity of material removal is the stability of the lithographically patterned transition metal layers following heat treatment. Ni was distinguished by its ability to remain localized without disruption of its structure. Thus, it catalyzed the conversion of C from sp^3 to sp^2 state. However, the transport and segregation of C in Fe, Co and FeCoB led to the disruption and dispersion of the TM particulates, which led to loss of specificity in material removal. The etched profiles deviated markedly from the lithographically patterned features. However, FeCoB stands out as an effective etchant due to the role of B in catalyzing the C removal in a microstructurally agnostic fashion. Growing from these observations, hierarchical etchants were designed, where bilayers of Ni and FeCoB were used to define gradients in material removal. Sloped etching profiles, where the angle can be modulated through a choice of heat treatment was demonstrated.

CRediT authorship contribution statement

Zhijie Wang: Conceptualization, Methodology, Validation, Investigation, Writing – original draft. **M. Ravi Shankar:** Conceptualization, Writing – review & editing, Supervision, Project administration, Funding acquisition.

Declaration of competing interest

The authors declare that they have no known competing financial interests or personal relationships that could have appeared to influence the work reported in this paper.

Data availability

Data will be made available on request.

Acknowledgements

Support from the II-VI Foundation Block Gift program and the National Science Foundation (1921842) are gratefully acknowledged.

Appendix A. Supplementary data

Supplementary data to this article can be found online at https://doi.org/10.1016/j.diamond.2022.109482.

References

[1] A.D. Matthew, J.E. Christopher, R.V. Rashmi, C.B. Brent, R.P. Steven, Application of precision diamond machining to the manufacture of microphotonics components, Proc.SPIE 5183 (2003) 94–108.
[2] E. Brinksmeier, R. Gläbe, L. Schönemann, Review on diamond-machining processes for the generation of functional surface structures, CIRP J. Manuf. Sci. Technol. 5 (1) (2012) 1–7.
[3] S. Gong, M.R. Shankar, Effect of microstructural anisotropy on severe plastic deformation during material removal at micrometer length-scales, Mater. Des. 194 (2020), 108874.
[4] J.M. Kenoyer, M. Vidale, A new look at stone drills of the Indus Valley tradition, MRS Online Proc. Libr 267 (1) (1992) 495–518.
[5] H. Umezawa, M. Nagase, Y. Kato, S.-I. Shikata, High temperature application of diamond power device, Diam. Relat. Mater. 24 (2012) 201–205.
[6] X. Zhang, T. Matsumoto, U. Sakurai, T. Makino, M. Ogura, S. Yamasaki, M. Sometani, D. Okamoto, H. Yano, N. Iwamuro, T. Inokuma, N. Tokuda, Energy distribution of Al2O3/diamond interface states characterized by high temperature capacitance-voltage method, Carbon 168 (2020) 659–664.
[7] J. Liang, A. Kobayashi, Y. Shimizu, Y. Ohno, S.-W. Kim, K. Koyama, M. Kasu, Y. Nagai, N. Shigekawa, Fabrication of GaN/Diamond heterointerface and interfacial chemical bonding state for highly efficient device design, Adv. Mater. 33 (43) (2021) 2104564.
[8] H. Luo, K.M. Ajmal, W. Liu, K. Yamamura, H. Deng, Atomic-scale and damage-free polishing of single crystal diamond enhanced by atmospheric pressure inductively coupled plasma, Carbon 182 (2021) 175–184.
[9] I. Akimoto, N. Naka, N. Tokuda, Time-resolved cyclotron resonance on dislocation-free HPHT diamond, Diam. Relat. Mater. 63 (2016) 38–42.
[10] H. Umezawa, Recent advances in diamond power semiconductor devices, Mater. Sci. Semicond. Process. 78 (2018) 147–156.
[11] N. Donato, N. Rouger, J. Pernot, G. Longobardi, F. Udrea, Diamond power devices: state of the art, modelling, figures of merit and future perspective, J. Phys. D. Appl. Phys. 53 (9) (2019), 093001.
[12] M. Kempkes, T. Zier, K. Singer, M.E. Garcia, Ultrafast nonthermal NV center formation in diamond, Carbon 174 (2021) 524–530.
[13] I. Aharonovich, E. Neu, Diamond nanophotonics, Advanced Optical Materials 2 (10) (2014) 911–928.
[14] A.V. Golovanov, V.S. Bormashov, N.V. Luparev, S.A. Tarelkin, S.Y. Troschiev, S. G. Buga, V.D. Blank, Diamond microstructuring by deep anisotropic reactive ion etching, physica status solidi (a) 215 (22) (2018) 1800273.
[15] Z. Zhang, H. Wu, L. Sang, J. Huang, Y. Takahashi, L. Wang, M. Imura, S. Koizumi, Y. Koide, M. Liao, Single-crystal diamond microelectromechanical resonator integrated with a magneto-strictive galfenol film for magnetic sensing, Carbon 152 (2019) 788–795.
[16] A.A. Martin, A. Bahm, J. Bishop, I. Aharonovich, M. Toth, Dynamic pattern formation in electron-beam-induced etching, Phys. Rev. Lett. 115 (25) (2015), 255501.
[17] T. Bi, Y. Chang, W. Fei, M. Iwataki, A. Morishita, Y. Fu, N. Niikura, H. Kawarada, C-si bonded two-dimensional hole gas diamond MOSFET with normally-off operation and wide temperature range stability, Carbon 175 (2021) 525–533.
[18] M.-L. Hicks, A.C. Pakpour-Tabrizi, R.B. Jackman, Diamond etching beyond 10 μm with near-zero micromasking, Sci. Rep. 9 (1) (2019) 15619.
[19] T.V. Kononenko, V.V. Kononenko, V.I. Konov, S.M. Pimenov, S.V. Garnov, A. V. Tishchenko, A.M. Prokhorov, A.V. Khomich, Formation of antireflective surface structures on diamond films by laser patterning, Applied Physics A 68 (1) (1999) 99–102.
[20] J. Riedrich-Möller, L. Kipfstuhl, C. Hepp, E. Neu, C. Pauly, F. Mücklich, A. Baur, M. Wandt, S. Wolff, M. Fischer, S. Gsell, M. Schreck, C. Becher, One- and two-dimensional photonic crystal microcavities in single crystal diamond, Nat. Nanotechnol. 7 (1) (2012) 69–74.
[21] M. Nagai, K. Nakanishi, H. Takahashi, H. Kato, T. Makino, S. Yamasaki, T. Matsumoto, T. Inokuma, N. Tokuda, Anisotropic diamond etching through thermochemical reaction between ni and diamond in high-temperature water vapour, Sci. Rep. 8 (1) (2018) 6687.
[22] V.G. Ralchenko, T.V. Kononenko, S.M. Pimenov, N.V. Chernenko, E.N. Loubnin, V. Y. Armeyev, A.Y. Zlobin, Catalytic interaction of fe, ni and pt with diamond films: patterning applications, Diam. Relat. Mater. 2 (5) (1993) 904–909.
[23] Y. Morofushi, H. Matsushita, N. Miki, Microscale patterning of single crystal diamond by thermochemical reaction between sidero-metal and diamond, Precis. Eng. 35 (3) (2011) 490–495.
[24] S. Jin, W. Zhu, T. Siegrist, T.H. Tiefel, G.W. Kammlott, J.E. Graebner, M. McCormack, Anisotropy in diamond etching with molten cerium, Appl. Phys. Lett. 65 (21) (1994) 2675–2677.
[25] W. Smirnov, J.J. Hees, D. Brink, W. Müller-Sebert, A. Kriele, O.A. Williams, C. E. Nebel, Anisotropic etching of diamond by molten ni particles, Appl. Phys. Lett. 97 (7) (2010), 073117.
[26] B. Gorowitz, R.J. Saia, Chapter 10 - reactive ion etching, in: N.G. Einspruch, D. M. Brown (Eds.), VLSI Electronics Microstructure Science, Vol. 8, Elsevier, 1984, pp. 297–339.
[27] C.J.H. Wort, R.S. Balmer, Diamond as an electronic material, Mater. Today 11 (1) (2008) 22–28.
[28] D.S. Hwang, T. Saito, N. Fujimori, New etching process for device fabrication using diamond, Diam. Relat. Mater. 13 (11) (2004) 2207–2210.
[29] M. Werner, Diamond metallization for device applications, Semicond. Sci. Technol. 18 (3) (2003) S41–S46.
[30] D. Rani, O.R. Opaluch, E. Neu, Recent advances in single crystal diamond device fabrication for photonics, sensing and nanomechanics, Micromachines 12 (1) (2021).
[31] Z. Wang, M.R. Shankar, Spatially selective, solid state etching of diamond using lithographically patterned FeCoB, Diam. Relat. Mater. 121 (2022), 108763.
[32] J. Wang, G. Zhang, N. Chen, M. Zhou, Y. Chen, A review of tool wear mechanism and suppression method in diamond turning of ferrous materials, Int. J. Adv. Manuf. Technol. 113 (11) (2021) 3027–3055.
[33] G. Jiang, Z. Jianguo, P. Yanan, K. Renke, N. Yoshiharu, S. Paul, Y. Xiaobin, W. Baorui, G. Dongming, A critical review on the chemical wear and wear suppression of diamond tools in diamond cutting of ferrous metals, International Journal of Extreme Manufacturing 2 (1) (2020), 012001.
[34] L. Zou, J. Yin, Y. Huang, M. Zhou, Essential causes for tool wear of single crystal diamond in ultra-precision cutting of ferrous metals, Diam. Relat. Mater. 86 (2018) 29–40.
[35] M.J. Burek, N.P. de Leon, B.J. Shields, B.J.M. Hausmann, Y. Chu, Q. Quan, A. S. Zibrov, H. Park, M.D. Lukin, M. Lončar, Free-standing mechanical and photonic nanostructures in single-crystal diamond, Nano Lett. 12 (12) (2012) 6084–6089.
[36] T.L. Liu, C.-J.C. Kim, Turning a surface superrepellent even to completely wetting liquids, Science 346 (6213) (2014) 1096.
[37] A. Yang, H. Imrane, J. Lou, J. Kirkland, C. Vittoria, N. Sun, V.G. Harris, Effects of boron addition to the atomic structure and soft magnetic properties of FeCoB films, J. Appl. Phys. 103 (7) (2008) 07E736.
[38] C.L. Platt, N.K. Minor, T.J. Klemmer, Magnetic and structural properties of FeCoB thin films, IEEE Trans. Magn. 37 (4) (2001) 2302–2304.
[39] G. Popovici, R.G. Wilson, T. Sung, M.A. Prelas, S. Khasawinah, Diffusion of boron, lithium, oxygen, hydrogen, and nitrogen in type IIa natural diamond, J. Appl. Phys. 77 (10) (1995) 5103–5106.
[40] B.S. El-Dasher, J.J. Gray, J.W. Tringe, J. Biener, A.V. Hamza, C. Wild, E. Wörner, P. Koidl, Crystallographic anisotropy of wear on a polycrystalline diamond surface, Appl. Phys. Lett. 88 (24) (2006), 241915.
[41] J.E. Field, The Properties of Diamond, Academic Press, London; New York, 1979.
[42] R.B. McLellan, The diffusion of boron in nickel, Scr. Metall. Mater. 33 (8) (1995) 1265–1267.